Parametric Subharmonic Instability of the Internal Tide at 29°N

J. A. MACKINNON,* M. H. ALFORD,+ OLIVER SUN,# ROB PINKEL,* ZHONGXIANG ZHAO,+ AND JODY KLYMAK@

* *Scripps Institution of Oceanography, La Jolla, California*
+ *Applied Physics Laboratory and School of Oceanography, University of Washington, Seattle, Washington*
# *Woods Hole Oceanographic Institution, Woods Hole, Massachusetts*
@ *University of Victoria, Victoria, British Columbia, Canada*

(Manuscript received 14 June 2011, in final form 6 September 2012)

ABSTRACT

Observational evidence is presented for transfer of energy from the internal tide to near-inertial motions near 29°N in the Pacific Ocean. The transfer is accomplished via parametric subharmonic instability (PSI), which involves interaction between a primary wave (the internal tide in this case) and two smaller-scale waves of nearly half the frequency. The internal tide at this location is a complex superposition of a low-mode waves propagating north from Hawaii and higher-mode waves generated at local seamounts, making application of PSI theory challenging. Nevertheless, a statistically significant phase locking is documented between the internal tide and upward- and downward-propagating near-inertial waves. The phase between those three waves is consistent with that expected from PSI theory. Calculated energy transfer rates from the tide to near-inertial motions are modest, consistent with local dissipation rate estimates. The conclusion is that while PSI does befall the tide near a critical latitude of 29°N, it does not do so catastrophically.

1. Introduction

a. Motivation

Internal tides provide one of the major dynamical pathways from large-scale energy in the ocean to small-scale turbulent dissipation and mixing. Internal tide generation occurs where the barotropic tide interacts with rough topography, the global patterns of which are relatively well known (Nycander 2005; Garrett and Kunze 2007). However, the geography of internal tide dissipation is not well quantified, mostly because of a lack of understanding of the waves' propagation and dynamical processes leading to wave breaking. Given that both regional and global climate models are sensitive to the distribution of the resultant diapycnal mixing (Harrison and Hallberg 2008; Jochum 2009; Jayne 2009), investigating the fate of the internal tide is a priority of the field.

The Internal Waves Across the Pacific (IWAP) experiment was designed in part to test the hypothesis that the tide loses significant energy through parametric subharmonic instability (PSI) near a critical latitude of 29°N, as predicted by the numerical simulation of MacKinnon and Winters (2005, hereafter MW). PSI involves transfer of energy from a propagating low-mode wave to two smaller-scale waves near half the frequency through nonlinear interaction (Müller et al. 1986). It has been documented near sites of both strong semidiurnal internal tides (Carter and Gregg 2006; Alford et al. 2007; Sun 2010) and diurnal internal tides (Alford 2008). MW suggested this mechanism would be particularly effective near 29°N, where the half-frequency "daughter" waves are close to the local inertial frequency, a natural resonant frequency of the ocean. Though the MW results showed catastrophic tidal decay, Hazewinkel and Winters (2011) note that expected PSI growth rates are often comparable to the time scales over which internal tides vary (spring-neap or otherwise), which may provide a natural upper bound to total instability growth.

Strong PSI could potentially be a important part of the global pattern of diapycnal mixing. Subharmonic waves tend to have smaller vertical scales (higher shear) and slow group velocities, making them likely to dissipate nearby. Simmons (2008) sees just such an effect in a global numerical simulation of the semidiurnal internal

Corresponding author address: J. A. MacKinnon, Scripps Institution of Oceanography, University of California, San Diego, 9500 Gilman Drive, La Jolla, CA 92093.
E-mail: jmackinn@ucsd.edu

DOI: 10.1175/JPO-D-11-0108.1

tide, although it less of a band than a series of localized mixing patches where strong internal tide beams cross 29°N or S. Additionally, any internal tide energy lost to PSI is not available to dissipate elsewhere in the ocean, so any attempt a global internal tide energy budget must take PSI into account.

b. Basic theory

Nonlinear energy transfer between internal waves has often been conceptualized with resonant wave–wave interaction theory. In this view, energy is transferred between a triad of weakly nonlinear waves through the first-order term of a perturbation expansion in wave amplitude (McComas 1977; Olbers 1983; Müller et al. 1986). The dynamical terms responsible for energy transfer are the quadratic terms in the equations of motion ($\mathbf{u} \cdot \nabla\mathbf{u}$, etc). The interaction is strongest when participating wavenumbers and frequencies satisfy simple resonance conditions,

$$\omega_1 \pm \omega_2 = \omega_0; \quad \mathbf{k}_1 \pm \mathbf{k}_2 = \mathbf{k}_0. \tag{1}$$

PSI refers to a subset of such interactions where the two so-called daughter waves (ω_1, ω_2) are both near half the frequency of the primary wave (ω_0). The interaction is thought to be particularly resonant at the latitude at which the half-frequency motions are exactly inertial (MW; Young et al. (2008)), which we refer to as a critical latitude, as it is a critical or turning latitude for the subharmonic (diurnal) waves. Unlike wind-generated near-inertial internal waves, which typically propagate downward from the surface, the daughter waves created by PSI have both up- and down-going energy. At this latitude (28.8 for the dominant M_2 internal tide and 29.9 for the secondary S_2 internal tide), the daughter waves are very close to inertial, and hence are expected to have vanishing vertical velocities and displacements. As a result, most of the quadratic energy transfer terms drop out, resulting in a relatively simple expression for energy input into one of the daughter waves:

$$\frac{\partial E_1}{\partial t} = -u_1^*\left(u_2^*\frac{\partial u_0}{\partial x} + v_2\frac{\partial u_0}{\partial y}\right) - v_1^*\left(u_2^*\frac{\partial v_0}{\partial x} + v_2^*\frac{\partial v_0}{\partial y}\right) + \text{c.c.}, \tag{2}$$

where the stars indicate complex conjugates, $E_1 = (u_1u_1^* + v_1v_1^*)/2$, and "c.c." denotes the complex conjugate of the whole expression, necessary to get a real energy transfer. An equivalent expression is found in Young et al. (2008) who pose the problem more generally as near-inertial instabilities of a horizontally uniform current oscillating at twice the local inertial frequency. Physically, (2) states that subharmonic motions draw energy from horizontal gradients in the primary wave, in this case the internal tide (MW). As Young et al. (2008) point out, this is at odds with a common dynamical view of PSI as forced by periodic modification of the buoyancy frequency by internal tide strain, though such a mechanism may be in play at lower latitudes.

When considered in a frame of reference aligned with the direction of propagation of the internal tide, (2) simplifies further to

$$\frac{\partial E_1}{\partial t} = -\frac{3}{2}ik_0u_1'^*u_2'^*u_0 + \text{c.c.}, \tag{3}$$

where k_0 is the horizontal wavenumber of the internal tide, and u' indicates horizontal velocity in the direction of internal tide propagation.

Before attempting to apply (3) to the data, we note several salient features. First, since the waves must satisfy wavenumber as well as frequency resonance, daughter waves with smaller vertical scales than the primary wave must have vertical wavenumbers of opposite signs. In other words, we expect one near-inertial daughter wave (u_1 or u_2) with phase that propagates upward in time, and one with downward phase propagation. This supposition will be exploited in simplifying the data analysis below. Second, it is impossible to directly calculate the horizontal internal tide wavenumber in (3) from time series data at a single location. A helpful step is to use the linear internal wave polarization relations to replace the horizontal internal tide velocity (u_0) with vertical internal tide velocity (w_0),

$$\frac{\partial E_1}{\partial t} = \frac{3}{2}im_0u_1'^*u_2'^*w_0 + \text{c.c.}, \tag{4}$$

where m_0 is now the vertical wavenumber of the internal tide. However, even though the internal tide horizontal wavenumber no longer explicitly appears, the crucial fact remains that (4) must be applied in a reference frame aligned with the propagation direction of the tide. This factor can be made explicit by rewriting the equation in terms of cardinal velocities

$$\begin{aligned}\frac{\partial E_1}{\partial t} &= \frac{3}{2}m_0\mathbf{u}_1^*\mathbf{u}_2^*w_0e^{i(2\theta_k+\pi/2)} + \text{c.c.} \equiv \Gamma e^{i(2\theta_k+\pi/2)} + \text{c.c.} \\ &\equiv |\Gamma|e^{i\theta_\Gamma}e^{i(2\theta_k+\pi/2)} + \text{c.c.},\end{aligned} \tag{5}$$

where θ_k is defined here to be the horizontal propagation direction of the internal tide CCW from due east, and $\mathbf{u}^* = (u + iv)^*$, where (u, v) are eastward and northward velocities. The factor of 2 in front of θ_k arises because both daughter wave velocities must go through coordinate frame rotation. For convenience we have

separated out a triple product term (Γ) and terms involving angles, including the factor of i from (4). Here, θ_Γ is the complex phase of the triple product Γ. Physically, there is a net energy transfer from the primary wave (the internal tide) to two subharmonic waves when (5) is positive. The term is maximized if the complex phase of the triple product Γ cancels the multiplying term,

$$\theta_\Gamma = -(2\theta_k + \pi/2). \quad (6)$$

The rate or strength of energy transfer depends on the magnitude of Γ averaged over time; nonnegligible time-averaged energy transfer occurs only if the three terms involved maintain a consistent sense of relative phase in time. Below we demonstrate that both of these requirements, a consistent triple product phase and a particular phase satisfying (6), are satisfied by the present data.

c. Outline

Here we present detailed evidence for PSI where an internal tide propagating north from Hawaii crosses 29°N. Preliminary results in Alford et al. (2007, hereafter A07) demonstrated that while there was clear evidence of PSI near 29°N, it did not catastrophically drain energy from the internal tide. Zhao et al. (2010) show further that the internal tide propagates significantly farther north without substantial loss of energy. Here we document the interaction between the internal tide and local high-mode near-inertial waves at 29°N, showing consistent phasing and positive, yet modest, estimated rates of energy transfer. Estimates of turbulent mixing rates are presented in a companion paper (MacKinnon et al. 2013). The remainder of the paper is organized as follows: section 2 describes the basic experimental design, section 3 describes basic properties of both near-inertial and semidiurnal waves, section 4 documents evidence for energy transfer between the two, and section 5 presents a discussion of results.

2. Experimental design

A series of observations were made during two cruises aboard R/V *Revelle* during spring 2006 spanning 60 days and 12 degrees of latitude (Fig. 1) (see the companion paper and A07 for more details). Here we focus on a 50-day moored time series at 28.9°N, mooring MP3, collected from 25 April to 13 June 2006. A McLane Moored Profiler on the mooring crawled from 85–1400 m every 1.5 h each way, measuring temperature, salinity, and horizontal velocity (Doherty et al. 1999). The profiler was equipped with an Acoustic Current Meter and CTD

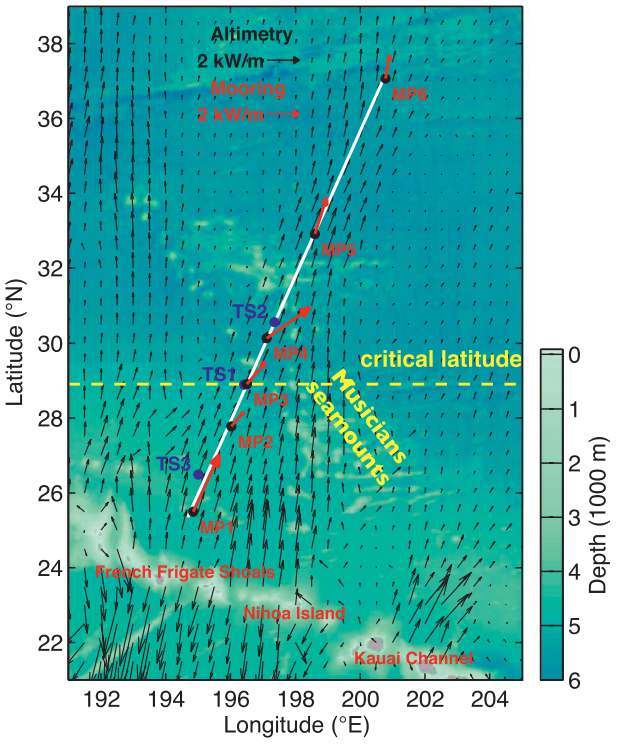

FIG. 1. Bathymetry (colors; axis at lower right), measurement locations (black, moorings; white, ship track), and internal-tide energy fluxes (black, altimetry estimates from Zhao and Alford (2009); red, mooring estimates from Zhao et al. (2010)). (top left) Reference arrows are shown; the M_2 critical latitude, 28.8°N, is indicated with a dotted line.

from Falmouth Scientific. Corrections were made for mismatched temperature and conductivity cells following Lueck and Picklo (1990). To remove residual sensor noise, temperature and conductivity data were smoothed to 3 m. Velocity data were smoothed to 10 m (increased noise associated with profiler motion begins to dominate at smaller scales, Alford 2010). A now-known firmware bug caused the profiler to go to sleep on 10 May (yearday 129), resulting in a one-day data gap for all variables.

All data were put into a semi-Lagrangian reference frame by referencing measurements on each isopycnal to the average resting depth of that isopycnal (Fig. 2). Vertical displacements were calculated by subtracting the time-mean density profile and dividing by a smoothed average buoyancy frequency profile. Vertical velocity was computed by time-differencing vertical displacement (Pinkel et al. 2012).

3. Observed wave properties

Velocity at MP3 is dominated by a combination of diurnal and semidiurnal signals (Fig. 2). Kinetic energy spectra show a large peak near the local inertial frequency

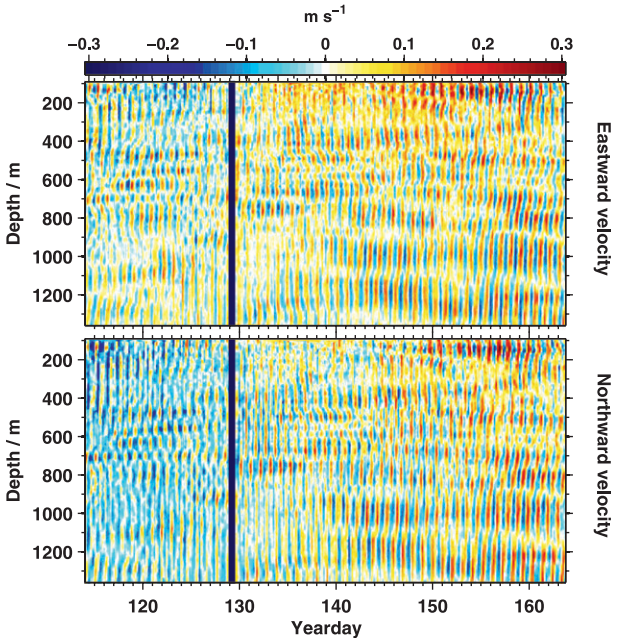

FIG. 2. Velocity in (top) the east–west and (bottom) north–south directions from the MP3 mooring, in a semi-Lagrangian (isopycnal following) reference frame. The yearday convention is such that noon on 1 January is yearday 0.5.

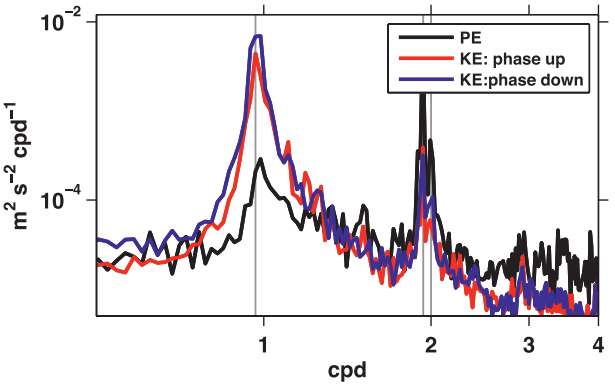

FIG. 3. Depth-averaged spectra of potential energy (black), horizontal kinetic energy with upward going phase (downward energy, red), and horizontal kinetic energy with downward gong phase (upward energy, blue) as a function of frequency. Inertial and semidiurnal (M_2, S_2) frequencies are indicated for reference by vertical gray lines.

and two distinct semidiurnal peaks at M_2 and S_2 (Fig. 3). For simplicity we refer to semidiurnal motions using the label D_2. As previously mentioned, the subharmonic frequency (D_2/2) is close to the local inertial frequency at this latitude, so the inertial shear may include a combination of PSI and wind-generated motions (A. Pickering 2012, personal communication). Before looking for evidence of nonlinear wave interactions, we separately discuss properties of the near-inertial and semidiurnal motions. In each case data have been bandpassed in the relevant frequency band with a fourth order Butterworth filter with passbands of (0.8–1.3) × f or M_2.

a. Near-inertial waves

Bandpassed near-inertial velocity shows a series of wave groups, as documented in more detail by A. Pickering (2012, personal communication) (Fig. 4). As described by A07, there are several periods with a "checkerboard" pattern of near-inertial velocity (e.g., near 600-m depth between yeardays 120 and 125), indicating the sum of upgoing and down-going waves. At other times (near 1000-m depth and yearday 155) phase clearly propagates upward in time, consistent with downward energy propagation. Near-inertial motions can be decomposed into motions that rotate CW and CCW with increasing depth by taking positive and negative quadrants of vertical Fourier transforms of (u + iv) at each point in time. According to the linear internal-wave polarization relations, a sense of CW rotation with increasing depth is consistent with phase that propagates upward with time (downward energy propagation), while CCW rotation is consistent with downward phase and upward energy propagation (Leaman and Sanford 1976). On average, there is comparable energy in motions with upward and downward phase (blue versus red in Fig. 3). Figure 4 (bottom two panels) shows the decomposed velocity fields. The observed sense of phase propagation with time for each one (i.e., up for CW and down for CCW) is indeed consistent with expectations, suggesting motions that can be considered quasi-linear internal waves. Over the 50 days of mooring measurement, multiple wave groups are clearly present. A run length test of either upward or downward near-inertial energy shows they are uncorrelated at time scales of 2.5 days or longer at the 5% level of significance (Gregg et al. 2003), a value that will be used in statistical significance calculations below.

b. Semi-diurnal waves

The internal tide at 29°N is a complex superposition of waves propagating different directions. Zhao et al. (2010) show that though there is a coherent north-bound mode-1 tide at the southernmost mooring (MP1), the further north one goes from the generation site the more complicated things become. In particular, at the latitude of MP3, the data shows comparatively larger amplitudes for higher modes (Zhao et al. 2010). A regional numerical internal tide simulation made with the POM model suggests higher mode internal tides have complex spatial structure, with some energy radiating from the local Musicians Seamounts. For example, modeled

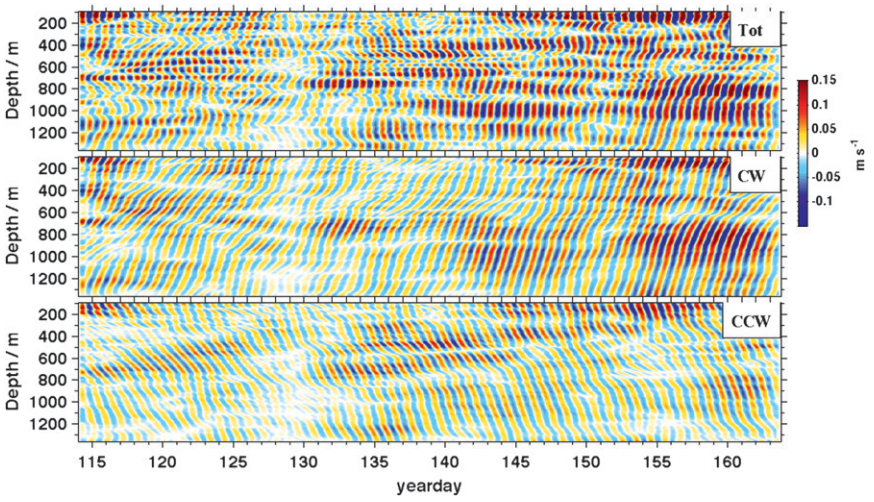

FIG. 4. (top) Northward component of bandpassed near-inertial velocity. (middle) The component of near-inertial velocity that rotates CW with depth, which according to the linear internal wave polarization relations should be consistent with motions that propagate upward in time, as visible in the figure. (bottom) Near-inertial velocity that rotates CCW with depth, consistent with downward phase propagation.

mode-3 fluxes show a pulse of energy propagating to the northwest near the mooring location (Fig. 6), although flux direction is highly variable near the mooring location. Given that these waves are expected to be significantly refracted by an evolving mesoscale (Rainville and Pinkel 2006), an effect not included in the POM model, detailed point comparisons between modeled and observed data are not pursued further here.

The complex depth and time structure of semidiurnal bandpassed velocity is shown in Fig. 5. There are several periods of relatively large north-south velocity, roughly consistent with the average northward energy flux observed at this site (vectors in Fig. 1). However, while internal tide flux is generally dominated by low modes, we expected motions with higher horizontal wavenumbers to contribute more to PSI [(3)]. For linear internal waves the horizontal wavenumber is simply proportional to the vertical wavenumber, so all else being equal we expect higher mode internal tides to be more susceptible to PSI. To apply (3) we need to know the direction of these higher-mode waves, the direction of the horizontal wave vector.

Pseudomomentum is a useful quantity for assessing internal tide wave-vector direction. For a linear propagating wave, pseudomomentum is the product of the vector horizontal wavenumber and the scalar wave action,

$$\mathbf{P} = \mathbf{k}_H A = \mathbf{k}_H \frac{E}{\omega} \tag{7}$$

where $\mathbf{k}_H$ is the horizontal wave vector, E is the energy density, and ω the intrinsic wave frequency. For relatively low-frequency internal waves ($\omega \ll N$), this can be calculated approximately as

$$\mathbf{P} \approx \left[\left\langle -\zeta \frac{du}{dz} \right\rangle, \left\langle -\zeta \frac{dv}{dz} \right\rangle \right], \tag{8}$$

where ζ is isopycnal displacement, u, v are eastward and northward wave velocities, and the average $\langle \cdot \rangle$ is taken over at least one wave period (Pinkel et al. 2012).

Pseudomomentum is calculated by applying (8) to D_2 bandpassed velocities and isopycnal displacements (as shown in Fig. 5). When applied to the full D_2 fields the result is noisy. Below we show bicoherence is strongest between near-inertial waves and an internal tide at vertical scales larger than a few hundred meters. Hence D_2 signals are smoothed to 200 m vertically before pseudomomentum is calculated. Pseudomomentum time series show consistent sense of direction in different depth ranges (Fig. 5, bottom two panels). For example, eastward pseudomomentum is generally positive above 800 m and negative below.

Time-averaged profiles of the eastward and northward components of **P** are shown (in Fig. 7, left panel), with the angle between them shown in the right panel. For propagating internal waves, the angle of the vector **P** tells you the angle of the horizontal wave-vector, $\theta_k = \theta_P$. An ad-hoc estimate of the vertical wavenumber in (5), m_0, can be calculated by doing a weighted average of vertical spectra of pseudomomentum, resulting in $m_0 \approx 0.0074 = 2\pi/850$ m. This is approximately the equivalent wavelength for the mode-3 internal tide, the modeled fluxes for which are shown in Fig. 6.

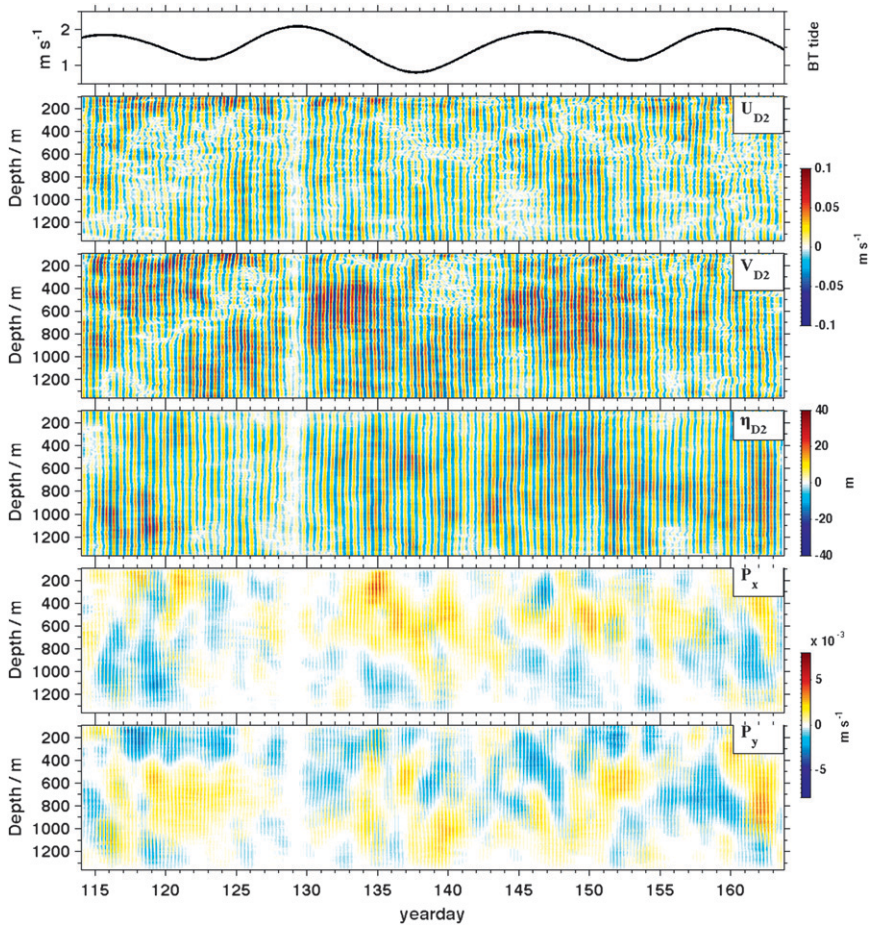

FIG. 5. (top) Magnitude of barotropic velocity at the mooring side, smoothed over 2 days. (middle three) Bandpassed semidiurnal eastward velocity, northward velocity, and vertical displacement, respectively, are shown. (bottom two) The eastward and northward component of pseudomomentum are shown.

The time-averaged semidiurnal pseudomomentum shows two depth ranges of relatively constant angle, highlighted in gray in Fig. 7. In the upper range (~400–750 m), the angle is consistent with a wave propagating slightly north of east, while in the lower depth range (~850–1250 m) the angle is consistent with a wave propagating to the northwest (cf. to Fig. 6). Below we use these estimates of tidal propagation direction (θ_k) to evaluate the net energy transfer rate (5).

4. Evidence for PSI

Alford et al. (2007) discuss qualitative evidence for PSI at this site, including vertically standing near-inertial motions and the increasing prevalence of near-inertial motions with upward energy propagation equatorward of 29N. Near-inertial waves with upward energy propagation may also be generated by reflection off the bottom (Garrett 2001), though waves with the relatively small wavelengths observed here propagate very slowly, requiring very long transit times to get back to the upper ocean. In some places near-inertial waves may also be generated as lee waves by mesoscale flows over topography, though that mechanism is not predicted to be important in this part of the Pacific (Nikurashin and Ferrari 2011).

A more quantitative approach involves looking for evidence of phase-locking between semidiurnal and inertial motions, and ultimately applying (5) using the tide propagation direction gleaned from the pseudomomentum profiles. We start with a statistical approach to look at the phasing between the three types of waves expected to participate in PSI—an internal tide, upward-going inertial waves, and downward-going inertial waves. Bandpassed time series reveal that all three types of waves show multiple wave groups present over the length of

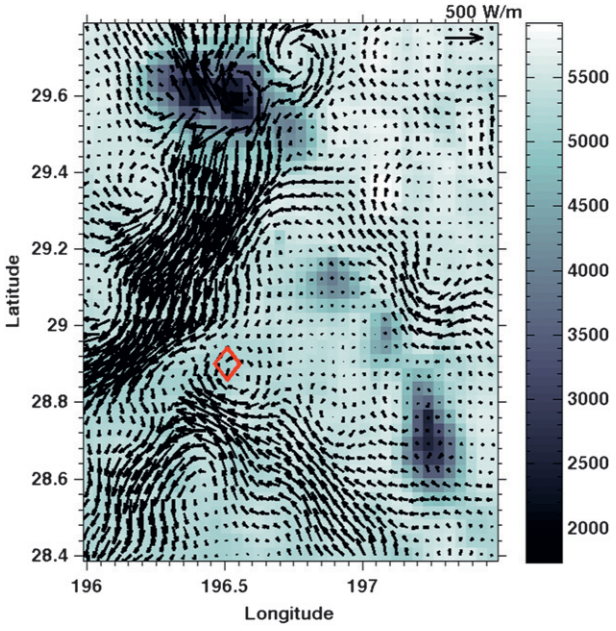

FIG. 6. Depth-integrated tidal energy fluxes from the POM model for mode-3. The model was initiated with horizontally uniform stratification and forced with a barotropic tide over approximately the region shown in Fig. 1. Scale arrows are shown in the upper right. The red diamond marks the location of the MP3 mooring. Gray-shaded contours indicate water depth, with seamounts visible to the north and east of the mooring. Courtesy of T.M.S. Johnston.

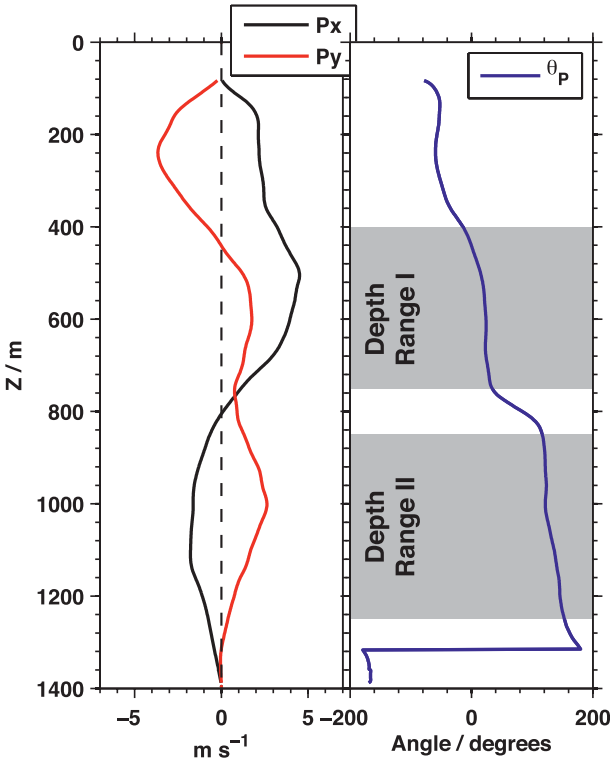

FIG. 7. (left) Time-averaged profiles of the eastward (black) and northward (red) components of vector pseudomomentum (8). (right) Angle of vector pseudomomentum, θ_P. In the text this angle is used as a proxy for the angle of internal tide propagation, $\theta_k \approx \theta_P$ in (5).

the observational record (Figs. 4 and 5), and the question becomes whether there is any constant sense of phasing between them over these multiple groups.

The bispectrum (Kim and Powers 1979; Elgar and Guza 1988) is a measure of consistent phase relationships between triads of waves that satisfy frequency and/or wavenumber resonance conditions [(1)]. Put another way, it's a method of evaluating (5) in Fourier space and determining whether there is any consistent sense of phasing between the internal tide and near-inertial waves. Bispectra are calculated as

$$B(\omega_1, \omega_2) = E[X^*_{\omega_1} X^*_{\omega_2} X_{\omega_1+\omega_2}], \qquad (9)$$

where $E[\cdot]$ is the expected value, and X represent complex FFTs of any variable of interest. Following (5), we choose the three variables to be horizontal velocity with a CW sense of rotation with depth (upward phase propagation), horizontal velocity with a CCW sense of rotation with depth (downward phase propagation), and vertical velocity. So the bispectrum as calculated here becomes

$$B(\omega_1, \omega_2) = E[\tilde{U}^*_{\text{up}}(\omega_1)\tilde{U}^*_{\text{down}}(\omega_2)\tilde{W}(\omega_1+\omega_2)], \qquad (10)$$

where the tilde indicates a Fourier transform. To compute bispectra, data are divided into half overlapping 5-day windows. Fourier transforms are taken of horizontal and vertical velocity in each window, at each depth, and applied to calculate B using (10). The expected value is calculated by averaging in both depth and time. Based on the results of Fig. 7 that the tide has two depth ranges of reasonably consistent propagation direction, bispectra are separately depth-averaged over these two depth ranges.

The results are plotted as a function of ω_1, ω_2 in Fig. 8 (left panels), for each of the depth ranges shown in Fig. 7. Here negative frequencies denote motions with a CW sense of rotation with time. Purely inertial motions are expected to appear as $\omega = -f = -1$ cpd, while higher frequency internal waves with elliptical hodographs will bleed onto positive frequencies as well. There is a strong magnitude of the bispectrum at $(-f, -f)$, meaning potentially significant interaction between two near-inertial waves and an internal tide (twice the frequency).

The significance of this tendency is assessed using bicoherence, defined as

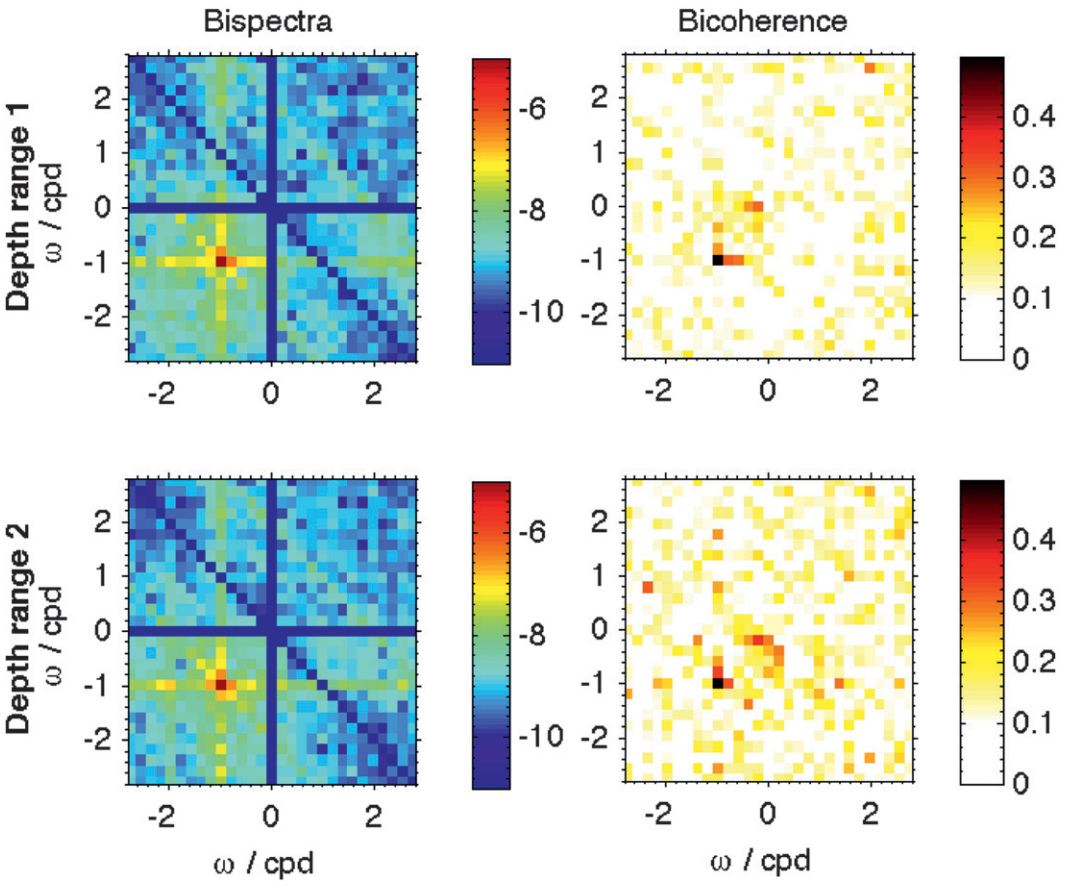

FIG. 8. (left) Absolute value of the bispectrum, as given by (10), for upper and lower depth ranges indicated in Fig. 7 (note the log scale for the colorbar). (right) Bicoherence for same depth ranges.

$$b^2(\omega_1, \omega_2) = \frac{|B(\omega_1, \omega_2)|^2}{E[|X_{\omega_1} X_{\omega_2}|^2] E[|X_{\omega_1+\omega_2}|^2]}, \qquad (11)$$

where again the X's represent U_{up}, U_{down}, and W respectively in our case. The bicoherence is normalized such that $0 \leq b \leq 1$. Here bicoherence is computed by taking the expected value over each indicated depth range, the result of which is shown in Fig. 8 (right panels). Elgar and Guza (1988) determine a 95% confidence level of $\sqrt{6/n_{\text{dof}}}$. Sun (2010) discusses bicoherence significance levels in some detail, and conclude that the appropriate number of degrees of freedom reflects the number of wave groups sampled, which is generally much smaller than the number of individual samples. Using a rough estimate that inertial phase and amplitude both change significantly about every 2.5 days and are coherent over about 100 m vertically (Fig. 4), we argue that the number of independent samples each of the two depth ranges used here (50 days and 350 vertical meters each) is $n_{\text{dof}} \approx 2 \times 20 \times 3$. This gives a 95% confidence level of 0.22. Given that the background noise level of Fig. 8 appears lower, this is likely a conservative estimate. The observed bicoherences at $(-f, -f)$ over this period are 0.52 for the upper depth range, and 0.54 for the lower depth range. The significance of the phase-locking between inertial and tidal motions is strong evidence of PSI and is one of the main results of this paper. In contrast, while there are other elevated regions of the bispectra, they do not appear bicoherent.

Bispectral techniques can also be used to look at triple product phasing in depth as well as time. In other words, bispectra can be computed as a function of vertical wavenumber in addition to frequency. Here we build on the results of frequency analysis and look at the vertical wavenumber bispectra specifically between near-inertial and semidiurnal motions,

$$B(m_1, m_2) = E[\tilde{U}^*_{ni}(m_1) \tilde{U}^*_{ni}(m_2) \tilde{W}_{D2}(m_1 + m_2)]. \qquad (12)$$

The resultant bicoherence is shown for each depth range in Fig. 9 (left panels). In both the upper and lower left panels there are a range of statistically significant bicoherences involving waves with oppositely signed vertical wavenumbers (upper left and bottom right quadrants). This is the theoretically predicted combination

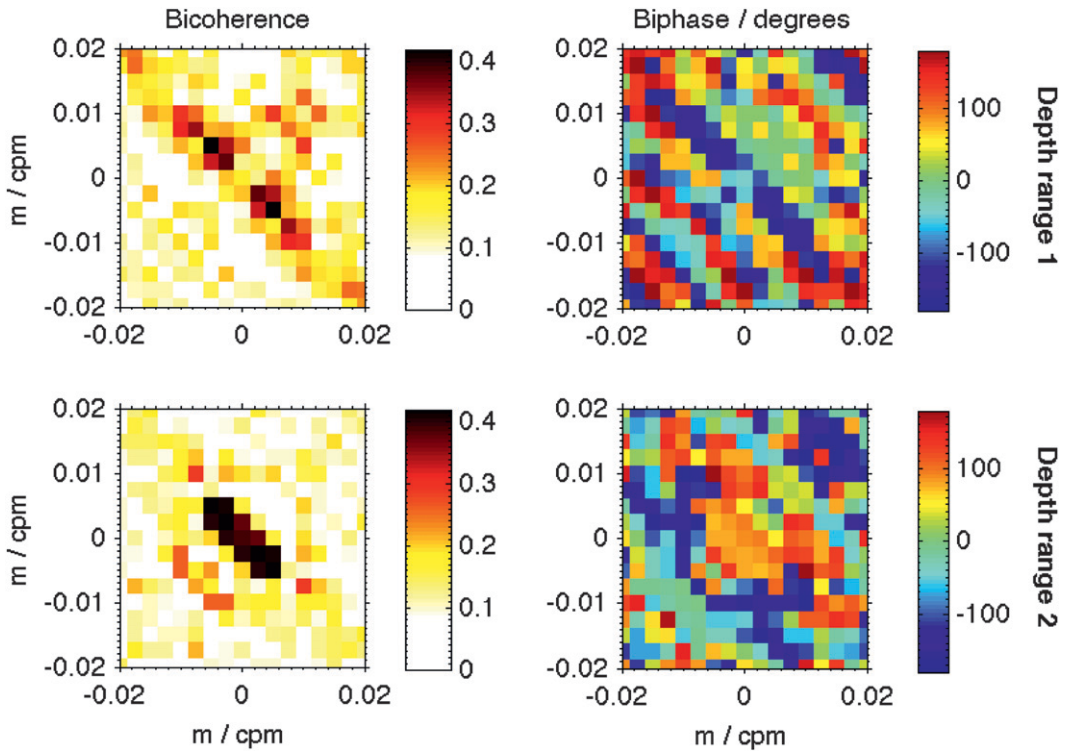

FIG. 9. (left) Bicoherence as a function of vertical wavenumber for ($-f$, $-f$, D2) frequency product for upper and lower depth ranges indicated in Fig. 7. (right) Biphase for same depth ranges.

of up-going and down-going near-inertial daughter waves. In the upper depth range the wavenumber of peak bicoherence is about 0.005 (200-m wavelength), while in the lower depth range the bicoherence shifts to lower wavenumbers, reflecting the larger vertical scales at depth visible in Fig. 4. The fact that the region of high bicoherence is close to a line with -1 slope suggests that the sum wavenumber ($m_1 + m_2$) is much less than that of either daughter wave, or in other words that the internal tide has larger vertical wavelengths than the inertial waves.

While both depth ranges indicated in Fig. 9 show bicoherence between inertial and tidal motions, the phase of the bispectrum is different between the two depth ranges. The right panels of Fig. 9 show biphase, the angle of (12), as a function of vertical wavenumber. In both the upper and lower panels the biphase has a consistent sign over the wavenumber range with significant bicoherence, but it is a different phase between the two panels.

A similar result can be seen slightly more intuitively by switching back to a time-domain analysis (Sun 2010). The triple produce, Γ from (5), is computed using band-passed time series of up-going near-inertial horizontal velocity, down-going near-inertial horizontal velocity, and semidiurnal vertical velocity. All time series have been vertically low-passed below 0.02 cpm, as suggested by the regions of bicoherence in Fig. 9. The absolute value and complex phase of Γ are shown in Fig. 10. Between about 400 and 800 m depth, there are three pulses of $|\Gamma|$ near year days 120,135, and 150 that roughly line up with the spring tides in the top panel of Fig. 5. In regions with strong magnitude of Γ (black contour), the angle is of one sense above about 800 m depth (blue) and of another sign below (red).

In fact, given that the internal tide has a different propagation direction in these two depth ranges (Fig. 7), one would expect the biphase to have a different sign in each depth range, through (5). The final step is to fully evaluate (5) combining the time-domain triple product, Γ and the tidal propagating angle, θ_k estimated from psuedomomenum. The result is plotted in the bottom panel of Fig. 10. Remarkably, it is positive almost everywhere, arguing for a steady energy transfer from the internal tide to near-inertial waves. The major exception, below 800 m between yeardays 145 and 150, is a time with a strong upward phase/downward energy packet visible in Fig. 4, which could be a wind generated wave.

The overall positive magnitude of (5) seen in Fig. 10 requires that the complex phase of Γ be balanced by the phase term in (5) related to tidal propagation (6). This can be seen explicitly by comparing the average angles, as done in the left panel of Fig. 11. Given the complexities of the wave field at this location, they are in

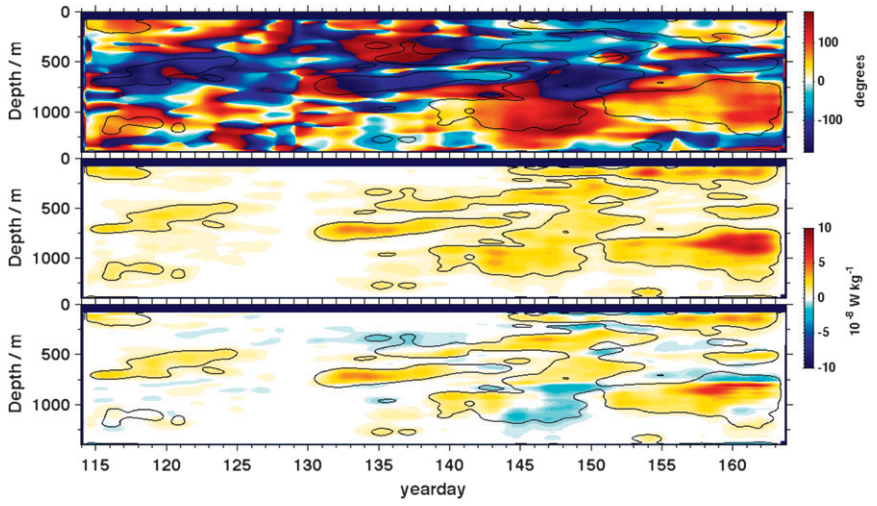

FIG. 10. (top) Complex phase and (middle) absolute value of the triple product Γ from (5). (bottom) The full energy transfer term from (5) is shown, where Γ has been multiplied by the phase term with the tidal direction given by pseudomomentum, $\theta_k \approx \theta_P$.

remarkably good agreement, with both showing consistent signs in the two depth ranges indicated. The time averaged rate of energy transfer is shown in the right panel. This is the estimated rate of energy transfer from the internal tide to near-inertial motions through PSI, and is the second major result of this paper. For reference, the average turbulent dissipation rate calculated by MacKinnon et al. (2013) is also shown.

5. Discussion and conclusions

The two most robust result of this work are 1) that there is a consistent, statistically bicoherent sense of phase between the internal tide and near-inertial waves as would only be expected when PSI is present, and 2) that the particular sense of that phase is one that leads to positive energy transfer from the internal tide to near-inertial waves.

The data show two depth ranges that have relatively consistent sense of semidiurnal pseudomomentum (Fig. 7). In each of these depth ranges, bispectral calculations in both frequency and wavenumber space show statistically significant phase-locking between three participating waves—an up-going near-inertial wave, a down-going near-inertial wave, and a semidiurnal internal tide. Using the tidal direction as estimated from psuedomomentum we calculate a net positive energy transfer from the internal tide to near-inertial daughter waves (Fig. 11). Though several previous studies have documented phase locking using bispectra (Carter and Gregg 2006; Sun 2010), to our knowledge this is the first study to explicitly calculate the energy transfer rates using an equation like (5).

As always with this type of calculation, care must be taken to not falsely conflate diurnal motions produced by PSI with those from either wind-generated waves or the diurnal internal tide. Wind generated waves would be expected to have primarily downward energy propagation (Alford et al. 2012). Diurnal internal tides would likely have similar vertical scales as the semidiurnal internal tides, not the high-mode structure of the diurnal motions discussed here. Most importantly, it is extremely unlikely that either wind or tidally generated diurnal motions would create features with exactly the right phase locking with the semidiurnal internal tide to indicate PSI.

The calculated magnitude of the energy transfer rate is quite modest, of roughly the same order as the local dissipation rates presented in the companion paper (Fig. 11). A rough time scale for subharmonic growth rate is given by the ratio of inertial energy (Fig. 4) to the tendency term, $\tau \sim E_{\rm ni}/(dE/dt)$. Taking the average either up- or down-going energy for $E_{\rm ni}$ and energy transfer rates from Fig. 11 gives time scales for growth of 2–5 days. Our estimate of the magnitude of the energy transfer rate is significantly more uncertain, reflecting uncertainty in all terms going into (5). One of the biggest uncertainties in the difficulty in estimating the direction of horizontal internal tide propagation direction in a complex wave field. When multiple waves are present with different propagation directions, the linear polarization relations and their byproducts (energy flux or pseudomomentum) become very difficult to interpret in a simple way (Nash et al. 2006; Martini et al. 2011).

The emerging story is that while PSI does befall a propagating internal tide, it does not do so in the

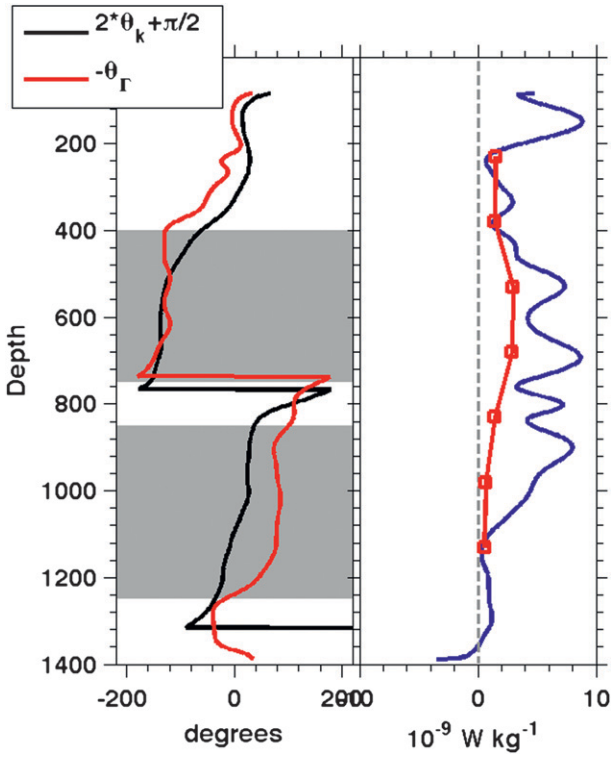

FIG. 11. (left) Comparison of expected and calculated triple product phase. Red line shows the negative of the angle of the calculated triple product, Γ in (5), while the black line shows the angle term in (5) using the direction of the semidiurnal pseudo-momentum as a proxy for the internal tide propagation direction. The agreement means that the product of the two terms in (5) is positive definite, leading to net positive energy transfer. (right) Time-averaged magnitude of energy transfer calculated using (5), in blue. Also shown is the average dissipation rate profile (red), reproduced from MacKinnon et al. (2013).

catastrophic way predicted by MW. Hazewinkel and Winters (2011) argue that the time scales for PSI growth are not much faster than the spring-neap cycle, so that truly catastrophic growth effectively cannot occur in any given spring tide. Based upon the results presented here, we believe that explanation is probably supplemented by the reasoning that 1) it is not mode-1 but closer to mode-3 internal tides that dominate energy transfer through PSI at this location, 2) these waves have geographically complex flux patterns that are likely to change with the evolving mesoscale as waves refract, and 3) time scales for PSI growth (2–5 days from these estimates) are comparable to typical synoptic time scales of mesosclale evolution. Truly catastrophic PSI growth simply does not have time to take hold. Further numerical simulations with more complex internal tide forcing, or observational studies in a location with a simpler internal tide, may provide further insight.

Jochum (2009) argues that even a moderate elevation associated with PSI at some latitudes may be an important mixing pattern to include in global models. Nevertheless, our results argue that the majority of internal tide energy escapes to dissipate in distant graveyards, the search for which is still ongoing.

Acknowledgments. This work was sponsored by NSF OCE 04-25283. We thank the tireless captain and crew of the R/V *Revelle*, for making our two months at sea productive and enjoyable. Eric Boget and Andrew Cookson played an essential role in the design, construction, deployment and recovery of the moorings. Tom Peacock, Paula Echeverri, and Kim Martini provided valuable assistance at sea. Shaun Johnston and Ed Zaron graciously conducted numerical simulations for our experiment. Many members of an ongoing ocean mixing Climate Process Team provided useful feedback and suggestions.

REFERENCES

Alford, M. H., 2008: Observations of parametric subharmonic instability of the diurnal internal tide in the South China Sea. *Geophys. Res. Lett.,* **35,** L15602, doi:10.1029/2008GL034720.

——, 2010: Sustained, full-water-column observations of internal waves and mixing near Mendocino Escarpment. *J. Phys. Oceanogr.,* **40,** 2643–2660.

——, J. A. MacKinnon, Z. Zhao, R. Pinkel, J. Klymak, and T. Peacock, 2007: Internal waves across the Pacific. *Geophys. Res. Lett.,* **34,** L24601, doi:10.1029/2007GL031566.

——, M. F. Cronin, and J. M. Klymak, 2012: Annual cycle and depth penetration of wind-generated near-inertial internal waves at Ocean Station Papa in the Northeast Pacific. *J. Phys. Oceanogr.,* **42,** 889–909.

Carter, G. S., and M. C. Gregg, 2006: Persistent near-diurnal internal waves observed above a site of M_2 barotropic-to-baroclinic conversion. *J. Phys. Oceanogr.,* **36,** 1136–1147.

Doherty, K., D. Frye, S. Liberatore, and J. Toole, 1999: A moored profiling instrument. *J. Atmos. Oceanic Technol.,* **16,** 1816–1829.

Elgar, S., and R. T. Guza, 1988: Statistics of bicoherence. *IEEE Trans. Acoust. Speech Signal Processes,* **36,** 1667–1668.

Garrett, C., 2001: What is the ''near-inertial'' band and why is it different from the rest of the internal wave spectrum? *J. Phys. Oceanogr.,* **31,** 962–971.

——, and E. Kunze, 2007: Internal tide generation in the deep ocean. *Annu. Rev. Fluid Mech.,* **39,** 57–87, doi:10.1146/annurev.fluid.39.050905.110227.

Gregg, M. C., T. B. Sanford, and D. P. Winkel, 2003: Reduced mixing from the breaking of internal waves in equatorial waters. *Nature,* **422,** 513–515.

Harrison, M., and R. Hallberg, 2008: Pacific subtropical cell response to reduced equatorial dissipation. *J. Phys. Oceanogr.,* **38,** 1894–1912.

Hazewinkel, J., and K. Winters, 2011: PSI of the internal tide on a beta-plane: Flux divergence and near-inertial wave propagation. *J. Phys. Oceanogr.,* **41,** 1673–1682.

Jayne, S. R., 2009: The impact of abyssal mixing parameterizations in an ocean general circulation model. *J. Phys. Oceanogr.,* **39,** 1756–1775.

Jochum, M., 2009: Impact of latitudinal variations in vertical diffusivity on climate simulations. *J. Geophys. Res.,* **114,** C01010, doi:10.1029/2008JC005030.

Kim, Y., and E. Powers, 1979: Digital bispectral analysis and its application to nonlinear wave interactions. *IEEE Trans. Plasma Sci.,* **PS-7,** 120–131.

Leaman, K. D., and T. B. Sanford, 1976: Observations on the vertical polarization and energy flux of near-inertial waves. *J. Geophys. Res.,* **6,** 894–908.

Lueck, R. G., and J. J. Picklo, 1990: Thermal inertia of conductivity cells: Observations with a Sea-Bird cell. *J. Atmos. Oceanic Technol.,* **7,** 756–768.

MacKinnon, J. A., and K. Winters, 2005: Subtropical catastrophe: Significant loss of low-mode tidal energy at 28.9 degrees. *Geophys. Res. Lett.,* **32,** L15605, doi:10.1029/2005GL023376.

——, M. H. Alford, R. Pinkel, J. Klymak, and Z. Zhao, 2013: The latitudinal dependence of shear and mixing in the Pacific transiting the critical latitude for PSI. *J. Phys. Oceanogr.,* **43,** 3–16.

Martini, K. I., M. H. Alford, E. Kunze, S. H. Kelly, and J. D. Nash, 2011: Observations of internal tides on the Oregon continental slope. *J. Phys. Oceanogr.,* **41,** 1772–1794.

McComas, C. H., 1977: Resonant interaction of oceanic internal waves. *J. Geophys. Res.,* **82,** 1397–1412.

Müller, P., G. Holloway, F. Henyey, and N. Pomphrey, 1986: Nonlinear interactions among internal gravity waves. *Rev. Geophys.,* **24,** 493–536.

Nash, J. D., E. Kunze, C. M. Lee, and T. B. Sanford, 2006: Structure of the baroclinic tide generated at Kaena Ridge, Hawaii. *J. Phys. Oceanogr.,* **36,** 1123–1135.

Nikurashin, M., and R. Ferrari, 2011: Global energy conversion rate from geostrophic flows into internal lee waves in the deep ocean. *Geophys. Res. Lett.,* **38,** L08610, doi:10.1029/2011GL046576.

Nycander, J., 2005: Generation of internal waves in the deep ocean by tides. *J. Geophys. Res.,* **110,** C10028, doi:10.1029/2004JC002487.

Olbers, D. J., 1983: Models of the oceanic internal wave field. *Rev. Geophys. Space Phys.,* **21,** 1567–1606.

Pinkel, R., L. Rainville, and J. Klymak, 2012: Semidiurnal baroclinic wave momentum fluxes at Kaena Ridge, Hawaii. *J. Phys. Oceanogr.,* **42,** 1249–1269.

Rainville, L., and R. Pinkel, 2006: Propagation of low-mode internal waves through the ocean. *J. Phys. Oceanogr.,* **36,** 1220–1236.

Simmons, H. L., 2008: Spectral modification and geographic redistribution of the semi-diurnal internal tide. *Ocean Modell.,* **21,** 126–138.

Sun, O., 2010: Subharmonic energy transfer from the semidiurnal internal tide at Kaena Ridge. Ph.D. thesis, University of California, San Diego, 109 pp.

Young, W., Y. Tsang, and N. Balmforth, 2008: Near-inertial parametric subharmonic instability. *J. Fluid Mech.,* **607,** 25–49.

Zhao, Z. and M. H. Alford, 2009: New altimetric estimates of mode-one M2 internal tides in the central North Pacific Ocean. *J. Phys. Oceanogr.,* **39,** 1669–1684.

——, ——, J. A. MacKinnon, and R. Pinkel, 2010: Long-range propagation of the semidiurnal internal tide from the Hawaiian Ridge. *J. Phys. Oceanogr.,* **40,** 713–736.